Synthesis and characterization of a flexible metal organic framework generated from MnIII and the 4,4′-bipyrazolate-ligand

S. Spirkl, M. Grzywa, Dirk Volkmer

Angaben zur Veröffentlichung / Publication details:

Spirkl, S., M. Grzywa, and Dirk Volkmer. 2018. "Synthesis and characterization of a flexible metal organic framework generated from MnIII and the 4,4′-bipyrazolate-ligand." *Dalton Transactions* 47 (26): 8779–86. https://doi.org/10.1039/c8dt01185k.

Synthesis and characterization of a flexible metal organic framework generated from Mn^{III} and the 4,4′-bipyrazolate-ligand†

S. Spirkl, M. Grzywa and D. Volkmer *

The synthesis and crystal structure of a novel metal organic framework, constructed from Mn^{III}, the 4,4′-bipyrazolate (BPZ) ligand and bridging hydroxyl groups is presented in this work. The network topology is identical to M-CFA-6 (M = Fe, Ga), but in the case of Mn-CFA-6, the structure crystallizes in the monoclinic crystal system due to the Jahn–Teller effect of the high spin d^4 manganese(III) centers. Thermal treatment of Mn-CFA-6 leads to decomposition of the framework above 150 °C. The porosity of Mn-CFA-6 was measured by carbon dioxide sorption, since solvent exchange and removal of the occluded solvent molecules leads to a compression of the pores. Electronic spectra of Mn-CFA-6 reveal two distinct absorption bands that are assigned to the two different manganese(III) centers as revealed by the single crystal structure analysis. Furthermore, SQUID measurements exhibit ferromagnetic behaviour of Mn-CFA-6 below the magnetic ordering at 45 K and antiferromagnetic coupling above this temperature. Evaluation of the paramagnetic region by the Curie-Weiß formula reveals an effective moment of 4.8μ_B, which is very close to the spin-only value of Mn^{III} centers.

Introduction

Many research groups are working on a steadily growing amount of different framework compounds, such as metal–organic frameworks (MOFs) or porous coordination polymers (PCPs), and secondary building units to study *e.g.*, the unique sorption properties,[1,2] the catalytic properties,[3–9] the application of MOFs for drug delivery,[10] the electrical conductivity,[11–13] magnetic properties[14] or just to enhance the specific surface area or pore size.[15,16] PCPs offer the possibility to stabilize metal centers in extraordinary oxidation states by occupation of free coordination sites of the metal center with appropriate bridging linker molecules and neutral or ionic co-ligands. This feature can be used either for catalytic studies,[17,18] but also for studies on the magnetic properties of special metal–ligand combinations. In this context, the magnetic exchange interaction of d-transition metal centers, such as manganese, in bridged unidirectional spin chains was found to be high for small bridges such as M–O–M or M–O–C–O–M, but also for M–OH–M.[14,19] Variation of the metal centers and thus tuning of the magnetic properties should offer a broad range of porous magnetic materials that might be used for magnetic separation, magnetic sensing as well as for low density magnets.[20,21]

In this work we present the synthesis of a microporous PCP, named **Mn-CFA-6**, which is built up from Mn^{III} centers, 4,4′-bipyrazolate ligands and bridging hydroxyl groups. The novel compound is structurally closely related to the CFA-6 frameworks but shows a Jahn–Teller distortion at the manganese centers, leading to a non-symmetric μ_2-bridging mode of the coordinated hydroxyl bridges and thus to a slightly smaller pore size and a different space group, compared to the currently characterized frameworks of CFA-6 type. To our knowledge, it is to date only the second metal organic framework which is demonstrated to contain Mn^{III} centers only, apart from $[Mn(OOCH)_3]$.[22]

To characterize the framework, single crystal structure analysis and X-ray powder diffraction methods were taken into account. Furthermore the thermal stability of the network was analyzed by thermogravimetric analysis and temperature dependent powder XRD measurements. After evacuation the porosity of the framework was determined by carbon dioxide sorption measurements, revealing a specific surface area of about 650 $m^2 g^{-1}$ and an estimated pore size of 3.8 Å. DR UV/vis/NIR spectroscopy reveals two transitions in the visible range. A unique feature of **Mn-CFA-6** is the existence of magnetically decoupled Mn^{III}–OH chains. This structural characteristic was utilized for

University of Augsburg, Institute of Physics, Chair of Solid State and Materials Chemistry, Universitätsstrasse 1, 86159 Augsburg, Germany.
E-mail: dirk.volkmer@physik.uni-augsburg.de; Fax: (+49) 821-598-5955

†Electronic supplementary information (ESI) available: Crystallographic data, BVS calculations. CCDC 1828453. For ESI and crystallographic data in CIF or other electronic format see DOI: 10.1039/c8dt01185k

studies on the magnetic properties of such manganese hydroxide chains. The valance state of Mn^{III} is further confirmed from temperature dependent susceptibility results.

Experimental

Materials and methods

The synthesis of the 4,4′-bipyrazole (H_2BPZ) was performed according to a slightly modified method previously reported.[23] All other chemicals were commercially available. The solvents were of analytical grade and further purification was not recommended. Fourier transform infrared spectroscopy in the range of 4000 to 400 cm^{-1} was performed with a Bruker Equinox 55 FT-IR spectrometer equipped with an ATR unit. Thermal analysis of the material was performed on a TA Instruments Q500, using alumina oxide crucibles. For this analysis a constant nitrogen flow of 100 mL min^{-1} was used while heating the sample from room temperature to 800 °C at a rate of 10 K min^{-1}. DR UV/vis/NIR spectra were measured from 2000 to 250 nm on a PerkinElmer λ 750 s spectrometer equipped with a Labsphere 60 mm RSA ASSY integrating sphere. Prior to the measurement Labsphere Spectralon SRS-99 was measured as a reference material. Afterwards 5 mg of the sample was prepared for measurement by thoroughly grinding with 45 mg of dry $BaSO_4$ in an agate mortar. Sorption properties of the material were determined by sorption experiments on an evacuated sample of **Mn-CFA-6** with high purity argon (99.999%, Linde AG) and nitrogen (99.999%, Linde AG) at 77 K performed with a Quantachrome Autosorb-1C. Carbon dioxide (99.999%, Linde AG) sorption at 195 K was measured on a BelSorpMax (Bel Inc.) sorption analyzer. For all sorption measurements the DMAc molecules inside the pores were exchanged with methanol by Soxhlet extraction. This was necessary to create porosity by solvent removal, due to the low thermal stability of **Mn-CFA-6**. Evacuation of the sample occurred at 100 °C for several hours.

Magnetic measurements

The temperature dependent dc magnetization (M) is carried out using a commercial Superconducting Quantum Interference Device (SQUID) Magnetometer (Quantum Design) equipped with a helium cryostat. Measurements were performed from 2 to 80 K.

PXRD techniques

Powder X-ray diffraction of the crystalline samples was performed on a Seifert XRD 3003 TT diffractometer equipped with a Meteor 1D detector. 40 kV, 40 mA, Cu Kα (λ = 1.54178 Å). The samples were carefully ground in an agate mortar, placed on a zero-background sample holder. Diffraction data was collected with a step size of 0.02° and a step time of 3.5 s per step in a 2Θ range between 5° and 65°. VT-XRD patterns of **Mn-CFA-6** were recorded on a Panalytical Empyrean diffractometer equipped with a Bragg-Brentano^{HD} mirror, PIXcel^{3D} 2 × 2 Detector using an XRK 900 reaction chamber by Anton Paar for measurements under inert gas. The diffraction patterns of the thoroughly ground sample were recorded from 5 to 70° 2Θ using a step size of 0.02° and a step time of 0.5 s. During the experiment the sample was treated with ultra-pure nitrogen gas (99.999%, Linde AG, flow rate 100 mL min^{-1}). After each measurement the sample temperature was raised in steps of 50 °C to 500 °C.

Single-crystal X-ray crystallography

Many attempts of the X-ray diffraction experiments on the crystals of **Mn-CFA-6·DMAc** have been performed. In most cases the crystals scattered very weakly and were heavily twinned (in many cases contained up to four domains). In all cases diffraction data of poor quality were obtained. The best recorded data were reordered for a single crystal of **Mn-CFA-6·DMAc** of approx. dimensions 14 × 17 × 31 μm^3 and resolution up to 1.2 Å (34.5° 2θ). X-ray data for the single crystal structure of **Mn-CFA-6·DMAc** were collected on a Bruker D8 Venture diffractometer. Intensity measurements were performed using monochromated (doubly curved silicon crystal) MoKα radiation (0.71073 Å) from a sealed microfocus tube. Generator settings were 50 kV, 1 mA. Data collection temperature was −173 °C. APEX3 software was used for preliminary determination of the unit cell.[24] Determination of integrated intensities and unit cell refinement were performed using SAINT.[25] The structure was solved and refined using the Bruker SHELXTL Software Package[26,27] and refined using SHELXL.[27,28] Selected crystal data and details of the structure refinement for **Mn-CFA-6·DMAc** are provided in Table 1. Non-

Table 1 Crystal data and structure refinement of **Mn-CFA-6·DMAc**

Compound	Mn-CFA-6·DMAc
Empirical formula	C_{10} H_{14} Mn N_5 O_2
Formula	$C_6H_5MnN_4O$, (C_4H_9NO)
M_r/g mol^{-1}	291.20
T/K	100(2)
Wavelength/Å	0.71073
Crystal system	Monoclinic
Space group	$C2/m$ (no. 14)
a/Å	12.911(3)
b/Å	14.712(3)
c/Å	6.6415(13)
β/°	115.41(3)
V/Å^3	1139.5(5)
Z	4
D_c/g cm^{-3}	1.697
μ/mm^{-1}	1.161
F(000)	600
θ range/°	2.769 to 19.983
Refls. collected	1808
Refls. unique	510
R(int)	0.16
Completeness to theta = 19.983°	90.1%
Refinement method	Full-matrix least-squares on F^2
Data/restraints/parameters	510/29/60
GooF	1.114
Final R indices [$I > 2\sigma(I)$][a]	R_1 = 0.1269, wR_2 = 0.3122
R indices (all data)[b]	R_1 = 0.1899, wR_2 = 0.3406
Largest diff. peak and hole	1.674 and −0.719 e Å^{-3}

[a] $R_1 = \sum||F_o| - |F_c||/\sum|F_o|$. [b] $wR_2 = \sum[w(F_o^2 - F_c^2)2]/\sum[w(F_o^2)2]^{1/2}$.

hydrogen atoms were refined with anisotropic temperature parameters. The hydrogen atoms were positioned geometrically and refined using a riding model. Complete crystallographic data for the structure reported in this paper have been deposited in the CIF format with the Cambridge Crystallographic Data Center, 12 Union Road, Cambridge CB21EZ, UK as supplementary publication no. CCDC 1828453.† Additionally for the freshly prepared powder sample and the dried powder sample, a Le Bail fit was performed by using the Jana2006 Program.[29] The XRPD pattern of Mn-CFA-6 is presented in Fig. S1,† the XRPD pattern of the dried sample is presented in Fig. S2 in the ESI.† The refined unit cell parameters of the freshly prepared sample are: a = 13.0786(3), b = 14.5700(4), c = 6.6617(2), β = 115.385(2), V = 1146.85(6). R_p = 1.24, wR_p = 2.20. The refined unit cell parameters of the dried sample are: a = 14.483(1), b = 6.2368(5), c = 11.4565(9), $\alpha = \beta = \gamma$ = 90, V = 1034.36(1). R_p = 1.24, wR_p = 2.20.

Synthesis

53.6 mg (0.2 mmol) of manganese(III)acetate dihydrate were placed in a Pyrex© tube. 53.6 mg (0.4 mmol) of 4,4′-bipyrazole, 4 mL of *N*,*N*-dimethylacetamide (DMAc) and 0.1 mL of 2,6-lutidine were added and the tube was capped. This reaction mixture was reacted in a preheated heating block under non-solvothermal conditions at 130 °C. After three days reaction time, the mixture was cooled to room temperature and the resulting red-brown crystals were filtrated, washed with 2 mL of DMAc and 2 mL of methanol, and dried in air.

Yield ([Mn(BPZ)(OH)]·DMAc): 12.3 mg (0.042 mmol) ~21% ATR IR bands: 3210 (br), 1620 (br), 1500 (s), 1412 (w), 1393 (w), 1378 (s), 1354 (w), 1318 (w), 1265 (s), 1240 (w), 1186 (w), 1161 (w), 1146 (vs), 1038 (vs), 1009 (s), 987 (w), 919 (vs), 826 (vs).

Due to the small pore size and the low thermal stability, the solvent could not be removed easily. Thus, for the sorption analysis the residual DMAc was exchanged by soxhlet extraction using pure methanol.

Results

Synthesis

The synthesis of **Mn-CFA-6** was performed under the same conditions as already applied for the synthesis of Fe-CFA-6. Therefore a trivalent metal salt was reacted under solvothermal conditions with the 4,4′-bipyrazole ligand under alkaline conditions to form the new network. Solely the yields of this reaction are significantly lower than for the synthesis of Fe-CFA-6. After the synthesis DMAc is stuck inside the pores, as can be seen from the infrared spectra. Due to the instability of **Mn-CFA-6** against water, the exchange of DMAc against methanol in a closed beaker was not successful, since Mn_3O_4 could be identified as a byproduct. To remove the solvent at mild conditions, the solvent was exchanged by Soxhlet extraction. To obtain suitable single crystals for X-ray diffraction several modifications of the synthesis conditions and reaction vessels were tested. Almost all crystals obtained by the given synthesis conditions showed typical signs of crystal twinning and scattered very weakly. Nevertheless, a single crystal suitable for SC X-ray diffraction study was finally found and used for an X-ray single crystal structure analysis.

Crystal structure analyses

A single crystal X-ray diffraction study reveals that **Mn-CFA-6** crystallizes in the monoclinic crystal system within the space group $C2/m$ (no. 12). The asymmetric unit consists of two manganese(III)-ions, half of the BPZ^{2-} ligand and one OH^- group. An ORTEP-style plot of the asymmetric unit of **Mn-CFA-6** with atom labels is shown in the ESI (Fig. S3†). The Mn(III) ions located at special positions (2/m, Wyckoff notation: 2a (Mn1) and 2c (Mn2)) are octahedrally coordinated. More precisely, the Mn^{III} coordination geometry involves four nitrogen atoms stemming from four BPZ^{2-} ligands in the equatorial plane and two OH^- groups in axial positions of a distorted octahedron. The BPZ^{2-} ligands and OH^- groups bridge the metal ions along linear chains of octahedrally coordinated manganese centers expanding in c-direction of the monoclinic crystal lattice. The 1D chains are connected by BPZ^{2-} ligands creating a 3D porous framework with one-dimensional rhombic channels running along the c-direction of the crystal lattice (see Fig. 1). This structure motif is similar to the one observed in the structures of Fe/Ga-CFA-6 published previously by our group.[30] However, in contrast to the isomorphous structures Fe/Ga-CFA-6, which crystallize in the orthorhombic crystal system, **Mn-CFA-6** crystallizes in the monoclinic crystal system. In our opinion the reason for this is the Jahn–Teller distortion that occurs for d^4 metal centers, *e.g.* manganese(III) centers, in high-spin state. In contrast to that, the d^5 configured high-spin iron(III) centers in Fe-CFA-6 cannot undergo a Jahn–Teller distortion owing to the symmetrical distribution of electrons in t_{2g} and e_g orbitals. As a result from this, the bond lengths in **Mn-CFA-6** vary significantly in comparison to Fe-CFA-6 and Ga-CFA-6. Consequently the Jahn–Teller distortion leads to a transformation of the unit cell from orthorhombic to monoclinic, which is accompanied by a slight compression of the 1D channels. Taking the van der Waals radii of hydrogen atoms (1.2 Å) into account, the channel diameter calculated between the hydrogen atoms of the OH^- groups is 5.5 Å. Estimation with the program SQUEEZE[31] reveals that the initial solvent-accessible void volume is 474.0 Å^3, which is 41.6% of the unit cell volume (1139.5 Å^3) for a probe radius of 1.68 Å, corresponding to the approximate van der Waals radius of argon.[32] The pores of the structure of **Mn-CFA-6** are occupied by disordered DMAc molecules. The positions of the DMAc molecules were impossible to resolve and refine from the electron density distribution. According to the crystallographic data there is an electron count of 192 per unit cell, which corresponds to four DMAc molecules in the unit cell of **Mn-CFA-6 DMAc**. The Mn–N and Mn–O distances are 2.107(19)–2.143(17) Å and 1.87(2)–2.25(2) Å, respectively. These values are in good agreement with those found in manganese(III) pyrazolate complexes and hydroxyl bridged manganese(III) complexes.[33,34] The atomic coordinates and isotropic thermal

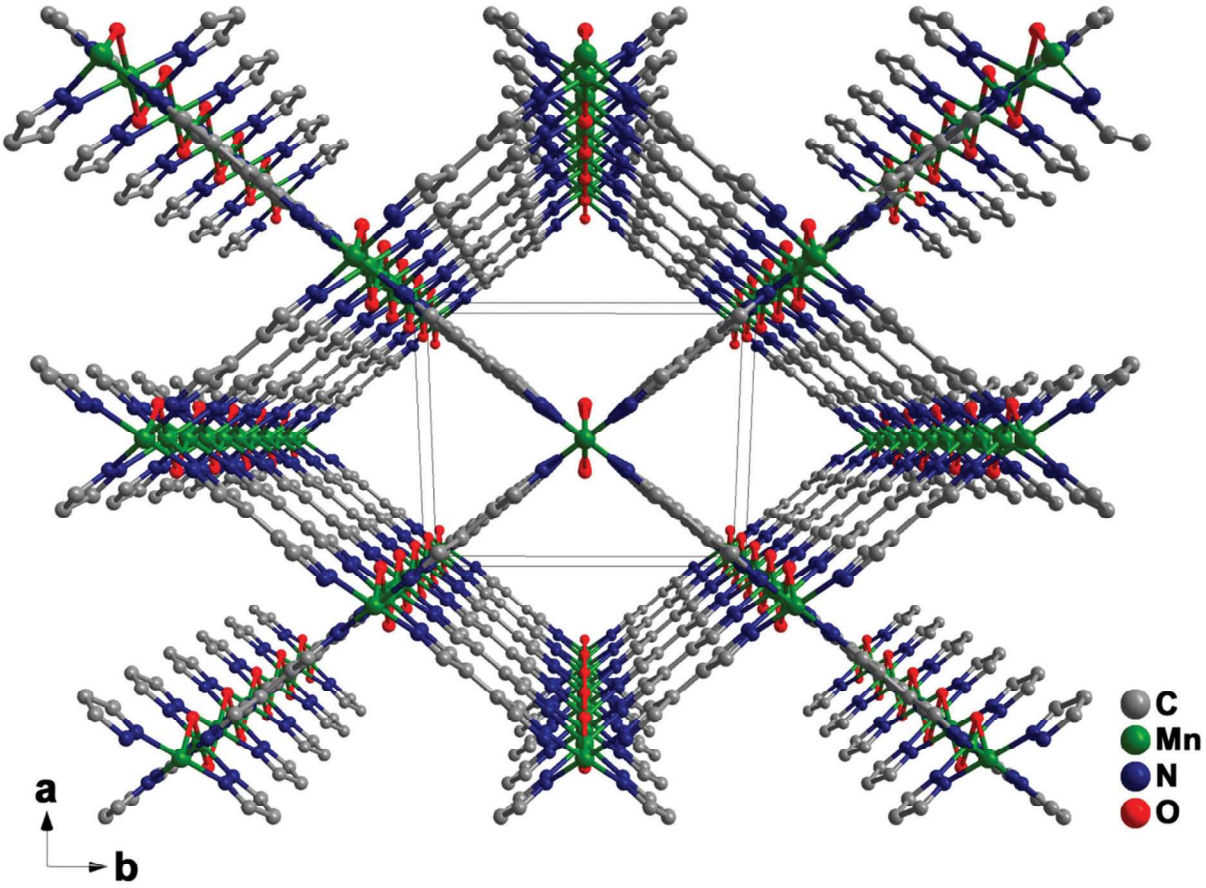

Fig. 1 Ball-and-stick crystal lattice model of **Mn-CFA-6**. Mn–OH–Mn chains along the crystallographic *c*-axis interconnected by the 4,4′-bipyrazolate ligands span the 3D network featuring 1D rhombohedral pores. (Hydrogen atoms are omitted for clarity.)

parameters, selected bond lengths and angles for **Mn-CFA-6·DMAc** are collected in Tables S1–3 in the ESI.†

From the single crystal structure determination it was not possible to characterize the bridging function, since hydrogen atoms have a very low electron density. Thus, in principle the bridging oxygen moiety might be an oxo, a hydroxo or an aquo group, corresponding to the possible oxidation states of +IV, +III or +II of the manganese centers that often occur in manganese coordination compounds. Bond lengths of representative compounds were compared with the Mn–N and Mn–O bond lengths found in **Mn-CFA-6**. The Mn–O distance in oxo bridged Mn^{IV}–O–Mn^{IV} complexes with nitrogen ligands is in between 1.743 and 1.84 Å, which does not fit the bond lengths from the single crystal data of our compound.[35–37] The Mn–O distance in similar Mn^{II}–OH–Mn^{II} compounds accounts to 2.021 and 2.09 Å, which would fit to the bond lengths of the Mn–O bonds in **Mn-CFA-6**.[38,39] In contrast to that, the bond length of Mn^{II}–N bonds in similar complexes are in between 2.171 and 2.364 and therefore significantly longer than the lengths of the Mn-N bonds in **Mn-CFA-6**. To determine the oxidation states of the manganese centers the distances between the metal centers and the ligand atoms may be evaluated by the bond valence method.[40] According to this method, the valence state of the metal centers can be estimated by the average bond lengths between the ligands and the metal centers in the present oxidation states and an empirical constant. In the case of **Mn-CFA-6** the bond valence sums of the two present manganese centers add up to 2.946 and 3.130. The bond valence sums for the cases of Mn^{II}, Mn^{III} and Mn^{IV} and parameters used for the calculations are shown in the Tables S4 and S5 in the ESI.†

Thermal analyses

Thermogravimetric analyses of **Mn-CFA-6** were performed with a freshly prepared sample of **Mn-CFA-6** from room temperature to 800 °C. The resulting TGA curve is shown in Fig. 2. From this measurement the evaporation of the solvent cannot be distinguished from the decomposition of the framework. Therefore the solvent was exchanged from DMAc to methanol by Soxhlet extraction. After the solvent exchange, another thermogravimetric analysis was performed to show that methanol could easily be removed from the pores. The result of this measurement is also shown in Fig. 2. This measurement shows a mass loss in the temperature range from room temperature to 50 °C. Afterwards a horizontal regime of the mass loss occurs, followed by a mass loss above 160 °C. This

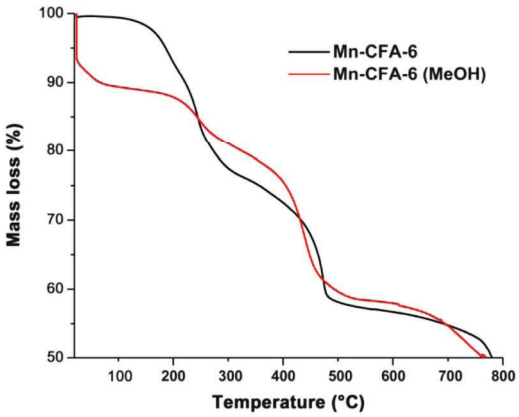

Fig. 2 Thermogravimetric analysis of **Mn-CFA-6** with DMAc inside the pores and with solvent-exchanged **Mn-CFA-6 (MeOH)** in the range of 25 to 800 °C under nitrogen atmosphere.

second step obviously shows the beginning of the decomposition of the framework.

To prove the findings from the thermogravimetric analysis, VT-X-ray powder diffraction measurements were performed. The sample was heated in steps of 50 °C to 500 °C. The resulting powder patterns are presented in Fig. 3. In the beginning there is no significant change in the diffraction patterns from room temperature to 100 °C. At 150 °C first changes in the diffraction pattern occur, *e.g.* a shift of the basal reflection to slightly higher values for 2Θ. Above 200 °C the powder patterns indicate a loss in crystallinity and only one broad reflection at around 11° 2Θ is present. Further heating of the sample to temperatures above 350 °C leads to the formation of new reflections. The resulting powder pattern of **Mn-CFA-6** at 500 °C was assigned to the powder pattern of MnO (PDF-No. 80-382) which implies the reaction of the Mn^{III} centers to Mn^{II} centers, that was similarly demonstrated for $K_3[Mn^{III}(C_2O_4)_3]$.[41] This finding is reasonable, due to the

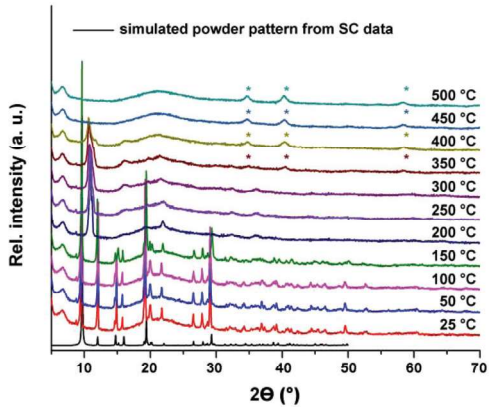

Fig. 3 VT-XRD patterns of **Mn-CFA-6** in the temperature range from 25 to 500 °C under nitrogen atmosphere. Above 350 °C a new phase (MnO, PDF-No. 80-382) is formed (asterisks). The black curve represents the simulated powder pattern from SC data.

reductive properties of the 4,4′-bipyrazolate ligand, that was found in the decomposition of Fe-CFA-6 under inert conditions.[30] Furthermore, Mn^{III} centers are known as oxidizing agents and are thus easily reduced.[42]

Sorption measurements

In order to determine the sorption properties of **Mn-CFA-6** a freshly prepared sample of solvent exchanged **Mn-CFA-6** was evacuated at 100 °C under reduced pressure. In sorption experiments with nitrogen or argon at 77 K, **Mn-CFA-6** did not show any gas uptake. Due to the solvent exchange with methanol the geometry of the lattice changes as can be seen from the PXRD patterns presented in Fig. S4 in ESI.† Thus, we assumed that the pore size of the evacuated **Mn-CFA-6** is much smaller than the pore size of Fe-CFA-6. Therefore, a carbon dioxide sorption measurement (see Fig. S5 in ESI†) was performed at 195 K after the pretreatment described above. Due to the higher measurement temperature, the gas diffusion into the pores is much faster due to enhanced Brownian molecular motion.[43] The specific surface area of **Mn-CFA-6** determined from the sorption data amounts to ~650 $m^2\ g^{-1}$ and the uptake of carbon dioxide at a relative pressure of $p/p_0 = 0.2037$ adds up to 137.90 mL g^{-1}, revealing a lower amount of gas uptake in **Mn-CFA-6** compared to Fe- and Ga-CFA-6. Furthermore, the pore size distribution of **Mn-CFA-6** was simulated using a NLDFT Monte Carlo Simulation method for carbon dioxide on carbon materials. This simulation revealed a single maximum in the pore size distribution at around 3.8 Å. These findings are consistent with the results obtained from the nitrogen and argon isotherms performed at 77 K, revealing absolutely no gas uptake and thus indicating a very small pore opening. After the sorption measurements, the evacuated sample was analyzed by powder XRD to determine structural changes. The unit cell parameters were determined by using indexing programs DICVOL04[44] and TREOR.[45] The obtained values were compared to the unit cell parameters that were determined from the SC structure solutions of **Mn-CFA-6** and Fe-CFA-6 (Table 2). This comparison reveals clearly that the overall dimensions of the unit cell are decreasing upon solvent removal by around 10%. Interestingly, solvent removal leads to a change of the crystal systems from monocli-

Table 2 Comparison of the unit cell parameters of **Mn-CFA-6** (SC), of the evacuated phase (DICVOL, TREOR) and of Fe-CFA-6

		Mn-CFA-6 desolvated		
	Mn-CFA-6 (SC)	DICVOL	TREOR	Fe-CFA-6 (SC)[30]
a (Å)	12.911	14.449(6)	14.499(5)	14.842
b (Å)	14.712	11.461(3)	11.457(3)	6.624
c (Å)	6.642	6.237(2)	6.2408(5)	11.747
α (°)	90	90	90	90
β (°)	115.41	90	90	90
γ (°)	90	90	90	90
V (Å^3)	1139.49	1032.1	1036.1	1154.93
		$M_{12} = 32.8$	$M_{12} = 24$	
		$F_{12} = 32.9$	$F_{12} = 31$	

nic to orthorhombic. These results support the assumption that in the case of **Mn-CFA-6** a change in geometry occurs, whereas for Fe- and Ga-CFA-6 no evidences for such flexibility effects were present.

DR UV/vis/NIR spectroscopy

The single crystal structure reveals that two crystallographically non-equivalent and structurally distinct types of manganese centers are present in the framework. According to the bond valence sums, both manganese centers should be in oxidation state +III. To undergird the data, diffuse refection UV/vis/NIR spectra were recorded from a freshly prepared sample of **Mn-CFA-6**. The resulting spectrum is shown in Fig. 4 and features a broad intense maximum due to CT transitions. Underneath this broad transition, a shoulder at ~15 600 cm^{-1} and a peak at ~22 500 cm^{-1} occur, representing the two different manganese centers. According to the Tanabe–Sugano diagram of d^4 transition metal centers in octahedral coordination environment, only the $E_g \rightarrow T_{2g}$ transition is allowed. Thus, the presence of two distinct bands in the region between 15 000 and 25 000 cm^{-1} in the UV/vis/NIR spectrum fits closely to the structure solution with two different types of manganese(III) centers obtained by diffraction methods. The transitions above 30 000 cm^{-1} are attributed to the $\pi \rightarrow \pi^*$ transitions of the ligand.

Magnetic properties

Dc susceptibility ($\chi = M/H$) as a function of magnetic field (H) is shown in Fig. 5 for magnetic field of 10 kOe in zero-field-cooled (ZFC) and field-cooled (FC) conditions. The susceptibility sharply increases below 45 K (T_C) like a ferromagnet. The ZFC-FC curves show a clear bifurcation below around 35 K, followed by another change in slope below 18 K. These results indicate complex history dependent magnetic nature of the sample below magnetic ordering T_C. The clear hysteresis in isothermal magnetization at 2 K (see inset of Fig. 5) confirms ferromagnetic interaction of this compound. The coercive field

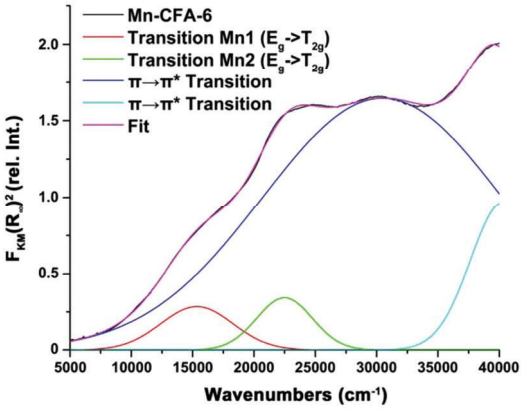

Fig. 4 DR UV/vis/NIR spectrum of **Mn-CFA-6**. The spectrum was fitted to determine the different absorption bands of the two Mn(III) centers. Above 30 000 cm^{-1} $\pi \rightarrow \pi^*$ transitions of the ligand are present.

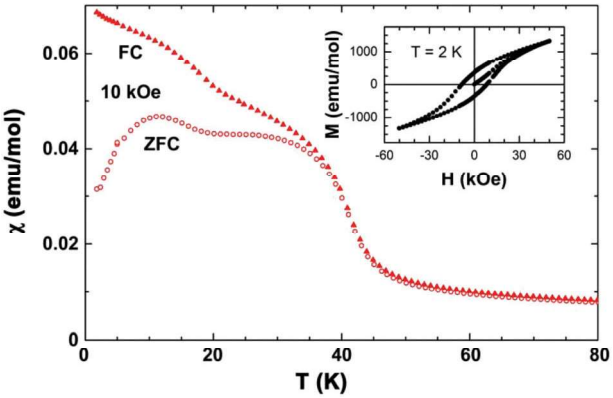

Fig. 5 Dc susceptibility as a function of temperature for 10 kOe magnetic field in ZFC-FC conditions. The inset shows the isothermal magnetization at 2 K.

is quite large in this compound, which in turns could result in ZFC-FC bifurcations in the anisotropic system. We have fitted $\chi(T)$ with the Curie–Weiss formula in the paramagnetic region which yields a Weiss temperature (Θ_P) of −360 K and an effective moment of $4.8\mu_B$. The effective moment is close to the spin-only value of Mn^{III}. The negative value of Θ_P indicates the presence of antiferromagnetic (AFM) interactions in this system. The isothermal magnetization also does not saturate at high magnetic field and rather varies linearly with increasing field, which is not a characteristic of a pure ferromagnet. The absolute value of the Weiss temperature is much higher than magnetic ordering, $\Theta_P > T_C$. Therefore, our results indicate towards canted AFM nature of this compound. Similar complex magnetism is observed in the compound CFA-12,[46] which is attributed to a canted antiferromagnet. Further detail magnetic results will be discussed elsewhere.

Conclusion

In this work we report the synthesis and characterization of a novel framework named **Mn-CFA-6**. The structure motif is closely related to the structures of Fe- and Ga-CFA-6 and the MIL-53 structure archetype. To date, the exclusive incorporation of Mn^{III} centers into metal organic frameworks is very challenging, due to the highly oxidizing nature of Mn^{III} centers and the resulting instability of manganese(III) compounds at ambient conditions. Consequently, the thermal analysis revealed a stability of up to 150 °C under nitrogen atmosphere. To remove the residual DMAc molecules (boiling point: 165 °C) occluding the pores of the framework, a solvent exchange with anhydrous methanol, using a Soxhlet extractor, was performed. The pore size of **Mn-CFA-6** is significantly smaller than the pore sizes of Fe- and Ga-CFA-6, thus carbon dioxide sorption measurements were necessary to determine the specific surface area. Evacuation of the solvent-exchanged framework under reduced pressure at 100 °C is accompanied by a collapse of the pores. Such breathing effects are well

known for the MIL-53 structures, whereas Fe- and Ga-CFA-6 did not show any breathing. The Jahn–Teller distortion of Mn^{III} centers leads to an asymmetric distortion of the hydroxyl bonds and, concomitantly, to a distortion of the unit cell. Thus, two crystallographically and structurally different manganese centers can be distinguished. In accordance to this, two different absorption bands evoked by the $E_g \rightarrow T_{2g}$ transitions of the Mn^{III} centers are found in the UV/vis/NIR spectrum of **Mn-CFA-6**. Determination of the magnetic properties revealed an antiferromagnetic interaction between the manganese centers and an oxidation state of +III according to the effective moment of $4.8\mu_B$, which is close to the effective moment of spin-only manganese(III) centers.

Conflicts of interest

There are no conflicts to declare.

Acknowledgements

Tathamay Basu is gratefully acknowledged for performing and interpreting the magnetic measurements. Dmytro Denysenko is acknowledged for fruitful discussions in terms of sorption analysis. This work was funded by the DFG priority program 1928 COORNETS (grant holder D. V., grant no. VO 829/12-1).

References

1 S. Krause, V. Bon, I. Senkovska, U. Stoeck, D. Wallacher, D. M. Többens, S. Zander, R. S. Pillai, G. Maurin, F. o.-X. Coudert and S. Kaskel, *Nature*, 2016, **532**, 348–352.
2 S. Keskin, T. M. van Heest and D. S. Sholl, *ChemSusChem*, 2010, **3**, 879–891.
3 Z. Wang, G. Chen and K. Ding, *Chem. Rev.*, 2009, **109**, 322–359.
4 D. Farrusseng, S. Aguado and C. Pinel, *Angew. Chem., Int. Ed.*, 2009, **48**, 7502–7513.
5 M. Tonigold, Y. Lu, B. Bredenkotter, B. Rieger, S. Bahnmuller, J. Hitzbleck, G. Langstein and D. Volkmer, *Angew. Chem., Int. Ed. Engl.*, 2009, **48**, 7546–7550.
6 A. Corma, H. García and F. X. Llabrés i Xamena, *Chem. Rev.*, 2010, **110**, 4606–4655.
7 A. M. Bohnsack, I. A. Ibarra, V. I. Bakhmutov, V. M. Lynch and S. M. Humphrey, *J. Am. Chem. Soc.*, 2013, **135**, 16038–16041.
8 Z. Wang and S. M. Cohen, *Chem. Soc. Rev.*, 2009, **38**, 1315–1329.
9 A. Henschel, K. Gedrich, R. Kraehnert and S. Kaskel, *Chem. Commun.*, 2008, 4192–4194.
10 P. Horcajada, C. Serre, M. Vallet-Regí, M. Sebban, F. Taulelle and G. Férey, *Angew. Chem., Int. Ed.*, 2006, **45**, 5974–5978.
11 L. Sun, T. Miyakai, S. Seki and M. Dinca, *J. Am. Chem. Soc.*, 2013, **135**, 8185–8188.
12 L. Sun, M. G. Campbell and M. Dinca, *Angew. Chem., Int. Ed.*, 2016, **55**, 3566–3579.
13 A. A. Talin, A. Centrone, A. C. Ford, M. E. Foster, V. Stavila, P. Haney, R. A. Kinney, V. Szalai, F. El Gabaly, H. P. Yoon, F. Léonard and M. D. Allendorf, *Science*, 2014, **343**, 66–69.
14 K. S. Asha, K. M. Ranjith, A. Yogi, R. Nath and S. Mandal, *Dalton Trans.*, 2015, **44**, 19812–19819.
15 O. K. Farha, I. Eryazici, N. C. Jeong, B. G. Hauser, C. E. Wilmer, A. A. Sarjeant, R. Q. Snurr, S. T. Nguyen, A. Ö. Yazaydın and J. T. Hupp, *J. Am. Chem. Soc.*, 2012, **134**, 15016–15021.
16 H. Deng, S. Grunder, K. E. Cordova, C. Valente, H. Furukawa, M. Hmadeh, F. Gándara, A. C. Whalley, Z. Liu, S. Asahina, H. Kazumori, M. O'Keeffe, O. Terasaki, J. F. Stoddart and O. M. Yaghi, *Science*, 2012, **336**, 1018–1023.
17 R. J. Comito, K. J. Fritzsching, B. J. Sundell, K. Schmidt-Rohr and M. Dincă, *J. Am. Chem. Soc.*, 2016, **138**, 10232–10237.
18 T. Zhang, K. Manna and W. Lin, *J. Am. Chem. Soc.*, 2016, **138**, 3241–3249.
19 P. Dechambenoit and J. R. Long, *Chem. Soc. Rev.*, 2011, **40**, 3249–3265.
20 D. Maspoch, D. Ruiz-Molina and J. Veciana, *J. Mater. Chem.*, 2004, **14**, 2713–2723.
21 R. J. Kuppler, D. J. Timmons, Q.-R. Fang, J.-R. Li, T. A. Makal, M. D. Young, D. Yuan, D. Zhao, W. Zhuang and H.-C. Zhou, *Coord. Chem. Rev.*, 2009, **253**, 3042–3066.
22 A. Cornia, A. Caneschi, P. Dapporto, A. C. Fabretti, D. Gatteschi, W. Malavasi, C. Sangregorio and R. Sessoli, *Angew. Chem., Int. Ed.*, 1999, **38**, 1780–1782.
23 I. Boldog, J. Sieler, A. N. Chernega and K. V. Domasevitch, *Inorg. Chim. Acta*, 2002, **338**, 69–77.
24 *APEX3*, Bruker AXS Inc., Karlsuhe, 2016.
25 *SAINT*, Bruker AXS Inc., Karlsuhe, 2015.
26 G. M. Sheldrick, *SHELXTL*, 2013.
27 G. M. Sheldrick, *Acta Crystallogr., Sect. A: Found. Crystallogr.*, 2008, **64**, 112–122.
28 G. M. Sheldrick, *Acta Crystallogr., Sect. C: Struct. Chem.*, 2015, **71**, 3–8.
29 V. Petříček, M. Dušek and L. Palatinus, *Z. Kristallogr. - Cryst. Mater.*, 2014, **229**, 345–352.
30 S. Spirkl, M. Grzywa, C. S. Zehe, J. Senker, S. Demeshko, F. Meyer, S. Riegg and D. Volkmer, *CrystEngComm*, 2015, **17**, 313–322.
31 A. Spek, *Acta Crystallogr., Sect. C: Struct. Chem.*, 2015, **71**, 9–18.
32 Quantachrome Autosorb, Odelzhausen, Quantachrome, 2009.
33 E. Manrique, A. Poater, X. Fontrodona, M. Sola, M. Rodriguez and I. Romero, *Dalton Trans.*, 2015, **44**, 17529–17543.
34 U. Bossek, H. Hummel, T. Weyhermüller, K. Wieghardt, S. Russell, L. van der Wolf and U. Kolb, *Angew. Chem.*, 1996, **108**, 1653–1656.

35 B. C. Schardt, J. A. Smegal, F. J. Hollander and C. L. Hill, *J. Am. Chem. Soc.*, 1982, **104**, 3964–3972.
36 D. Brazzolotto, F. G. Cantú Reinhard, J. Smith-Jones, M. Retegan, L. Amidani, A. S. Faponle, K. Ray, C. Philouze, S. P. de Visser, M. Gennari and C. Duboc, *Angew. Chem., Int. Ed.*, 2017, **56**, 8211–8215.
37 R. Gupta, T. Taguchi, B. Lassalle-Kaiser, E. L. Bominaar, J. Yano, M. P. Hendrich and A. S. Borovik, *Proc. Natl. Acad. Sci. U. S. A.*, 2015, **112**, 5319–5324.
38 D. Tetard, A. Rabion, J.-B. Verlhac and J. Guilhem, *J. Chem. Soc., Chem. Commun.*, 1995, 531–532, DOI: 10.1039/C39950000531.
39 N. Kitajima, U. P. Singh, H. Amagai, M. Osawa and Y. Morooka, *J. Am. Chem. Soc.*, 1991, **113**, 7757–7758.
40 D. I. Brown, *The Chemical Bond in Inorganic Chemistry*, Oxford University Press, 2nd edn., 2002.
41 K. Nagase, *Bull. Chem. Soc. Jpn.*, 1973, **46**, 144–146.
42 R. C. Schothorst, O. O. Schmitz and G. Den Boef, *Anal. Chim. Acta*, 1986, **179**, 299–305.
43 D. Lozano-Castelló, D. Cazorla-Amorós and A. Linares-Solano, *Carbon*, 2004, **42**, 1233–1242.
44 A. Boultif and D. Louer, *J. Appl. Crystallogr.*, 2004, **37**, 724–731.
45 P.-E. Werner, L. Eriksson and M. Westdahl, *J. Appl. Crystallogr.*, 1985, **18**, 367–370.
46 T. Basu, A. Jesche, B. Bredenkotter, M. Grzywa, D. Denysenko, D. Volkmer, A. Loidl and S. Krohns, *Mater. Horiz.*, 2017, **4**, 1178–1184.